Coupled Southern Ocean cooling and Antarctic ice sheet expansion during the middle Miocene

Thomas J. Leutert[1*†], Alexandra Auderset[2,3], Alfredo Martínez-García[2], Sevasti Modestou[1] and A. Nele Meckler[1]

[1]Bjerknes Centre for Climate Research and Department of Earth Science, University of Bergen, Bergen, Norway

[2]Max Planck Institute for Chemistry, Mainz, Germany

[3]Geological Institute, ETH Zurich, Zurich, Switzerland

[*]E-mail: Thomas.Leutert@mpic.de

[†]Present address: Max Planck Institute for Chemistry, Mainz, Germany

The middle Miocene climate transition (~14 million years ago) was characterized by a dramatic increase in the volume of the Antarctic ice sheet. The driving mechanism of this transition remains under discussion, with hypotheses including circulation changes, declining carbon dioxide in the atmosphere and orbital forcing. Southern Ocean records of planktic foraminiferal Mg/Ca have previously been interpreted to indicate a cooling of 6-7°C and a decrease in salinity preceding Antarctic cryosphere expansion by up to ~300 thousand years. This interpretation has led to the hypothesis that changes in meridional heat and vapour transport along with an early thermal isolation of Antarctica from extrapolar climates played a fundamental role in triggering ice growth. Here, we revisit the middle Miocene Southern Ocean temperature evolution using

clumped isotope and lipid biomarker temperature proxies. Our records indicate that the Southern Ocean cooling and the associated salinity decrease occurred in phase with the expansion of the Antarctic ice sheet. We demonstrate that the timing and magnitude of Southern Ocean temperature change seen in previous reconstructions can be explained if we consider pH as an additional, non-thermal control on foraminiferal Mg/Ca ratios. Therefore, our new dataset challenges the view of a thermal isolation of Antarctica preceding ice sheet expansion, and suggests a strong coupling between Southern Ocean conditions and Antarctic ice volume in times of declining atmospheric carbon dioxide.

Proxy records of atmospheric carbon dioxide (CO_2) suggest that some of the highest CO_2 levels of the Neogene were reached during the warmth of the Miocene climatic optimum (~17-14 Ma)[1–3] making it a useful analogue for future climate projections. This climatic optimum was followed by a major shift in global climate[4,5]. The middle Miocene climate transition (MMCT) was marked by an increase in the volume of the Antarctic ice sheet causing a global sea level drop of around 40 to 90 m[6–8], and by a decline in atmospheric CO_2 of ~100-300 ppm[1–3]. The available temperature reconstructions based on Mg/Ca ratios in planktic foraminifera from the Atlantic and Pacific sectors of the Southern Ocean show an abrupt cooling of ~6-7°C that precedes the increase in ice volume by ~100-300 kyr[9,10]. Consequently, it has been suggested that an early thermal isolation of Antarctica played a fundamental role in sustaining long-term boundary conditions required for substantial ice build-up[9–11]. The observed decoupling of high latitude upper ocean temperatures and Antarctic ice volume was related to orbitally forced ocean and atmospheric circulation changes impacting meridional heat/vapour transport, with atmospheric CO_2 only playing a secondary role.

However, it has been shown that Mg/Ca ratios in foraminifera are not only controlled by calcification temperature but also by seawater Mg/Ca, salinity, and arguably pH[12,13]. These non-thermal influences introduce fundamental uncertainties in the use of Mg/Ca as a paleothermometer for the middle Miocene, where seawater carbonate chemistry appears to have been highly variable[2]. Therefore, independent reconstructions of Southern Ocean temperatures during the MMCT are of vital importance to better understand forcings and feedbacks in a rapidly changing climate system, and to address key questions such as the sensitivity of the Antarctic cryosphere to large changes in atmospheric CO_2[9,11].

Estimates of middle Miocene high latitude temperatures

Here, we shed light on Southern Ocean temperature evolution by applying two new independent paleothermometers at the site of one of the existing Mg/Ca records, Ocean Drilling Program (ODP) Site 1171 (48°30'S, 149°07'E, 2150 m water depth) on the South Tasman Rise[14]. We combine upper ocean temperature reconstructions based on clumped isotope (Δ_{47}) signatures in the planktic foraminifer *Globigerina bulloides* and isoprenoid glycerol dialkyl glycerol tetraether (GDGT) lipid ratios (TEX_{86}), in order to provide improved constraints on the magnitude and phasing of middle Miocene cooling. The carbonate clumped isotope method utilizes the temperature-dependence of the bonding between two heavy isotopes within carbonate molecules. The thermodynamic basis of this method implies that the proxy is largely unaffected by non-thermal factors[15]. While requiring large samples due to inherent analytical uncertainty, the clumped isotope method allows for accurate temperature reconstructions independent of seawater chemistry or biological effects[16–18]. The TEX_{86} paleothermometer is based on the temperature-dependence of the number of cyclopentane rings of GDGT membrane lipids produced by marine Thaumarchaeota[19]. The temperature sensitivity of these compounds derives from the biogeochemical regulation of their synthesis

by certain groups of archaea, which allows them to keep the membrane in a liquid-crystalline state and preserve its function at different temperatures[20]. TEX_{86}-estimated temperatures are also insensitive to changes in salinity and pH[21]. In some environments, additional inputs of isoprenoidal GDGTs from non-marine Thaumarchaeota sources could influence the estimated upper ocean temperature. However, the analysis of GDGT distributions on the samples from Site 1171 indicates that upper ocean temperature is the main driver of the observed TEX_{86} trends (Supplementary Information). The two proxies used in this study have very complementary strengths and weaknesses, with one (Δ_{47}) providing high fidelity absolute temperature constraints, albeit with inferior precision compared to other proxies, and the other (TEX_{86}) allowing detailed reconstruction of the temporal evolution of temperature changes.

At present, Site 1171 is located to the south of the Subtropical Convergence separating warm, saline subtropical waters from comparably cold and fresh subantarctic water masses[22] (Fig. 1, see also Supplementary Figs. S1 and S2). During the middle Miocene, the location of Site 1171 is estimated to have been further south (e.g., at ~53°S around 14 Ma) compared to its modern location[23,24], making it well-suited to study the evolution of Antarctic Circumpolar Current (ACC) and Southern Ocean frontal systems during the MMCT. We note that Site 1171 has migrated northward across the time interval of this study (roughly 1° from 15 Ma to 12 Ma)[23,24]. Therefore, long-term cooling at high southern latitudes may be slightly underestimated. Our clumped isotope temperature reconstruction is based on the planktic foraminifer species *G. bulloides*, which calcifies predominantly during austral spring[9,25,26] in the upper water column (~200 m water depth)[27] and is present throughout the middle Miocene sequence at Site 1171. Another reason to use *G. bulloides* is to enable a direct comparison of our results with existing Mg/Ca-based temperatures measured on the same species from this

100 site[9]. Our revised age model for Site 1171 uses nine magnetostratigraphic datums and four
101 carbon isotope datums (Supplementary Information).
102
103 In line with previous reconstructions[9,10,28] and recent modelling evidence[8,29], our
104 paleotemperature estimates (Fig. 2) are significantly higher than today's Southern Ocean
105 temperatures (modern austral spring temperature of ~5-8°C near the reconstructed
106 paleolatitude of Site 1171, Supplementary Fig. S1). In terms of overall temperature change,
107 we observe reasonable agreement between all proxies at Site 1171 when comparing the start
108 and the end of the investigated time period (see also Supplementary Fig. S5). However, both
109 the Δ_{47} and TEX_{86} records do not exhibit the abrupt cooling step of 6-7°C, which is indicated
110 by the Mg/Ca proxy between 14.2 and 13.9 Ma and thus starting before Antarctic cryosphere
111 expansion (Fig. 2). Instead, Δ_{47} and TEX_{86} suggest a more gradual long-term cooling during
112 the middle Miocene**.** Δ_{47}-based upper ocean temperatures vary between around 12 and 15°C
113 during the warmest part of the study interval during the Miocene climatic optimum
114 (around 14 Ma), and then decrease to ~10-12°C after the MMCT. In terms of overall trends
115 and timing, the TEX_{86}-based temperature record broadly mirrors the clumped isotope record.
116 Absolute temperatures from TEX_{86} and Δ_{47} are very similar when using the subsurface
117 calibration of Ho and Laepple[30], but the choice of the temperature calibration for TEX_{86} can
118 have a large effect on calculated temperatures (Supplementary Fig. S5). Therefore, we focus
119 our interpretation on the trends and timing of change in the TEX_{86}-based temperature record,
120 which are largely independent of the calibration used.
121
122 Δ_{47} compositions of well-preserved planktic foraminifera yield accurate deep-time
123 temperature estimates (albeit with comparably large analytical uncertainties), owing to their
124 insensitivity to ocean chemistry (over the range of natural variation in the upper waters of the

125 open ocean) and a lack of discernible vital effects[16–18]. However, foraminifera might be
126 subjected to post-depositional alteration, which can lead to a cold bias in upper ocean
127 temperatures derived from planktic foraminifera[17]. Scanning electron microscope images of
128 middle Miocene *G. bulloides* at Site 1171 indicate generally good preservation with no signs
129 of significant recrystallization and at most minor diagenetic calcite overgrowths and/or
130 dissolution, suggesting that diagenetic effects on primary geochemical signatures are small[17]
131 (Supplementary Information). This is in line with Shevenell et al.[9] finding no evidence of a
132 diagenetic bias in *G. bulloides* Mg/Ca values at Site 1171. Although we cannot exclude a
133 slight diagenetic cool bias of 1-2°C in our Δ_{47}-based temperatures, it would not affect the
134 main conclusions of this study (Supplementary Fig. S5). The good correspondence of the
135 temporal trends from TEX_{86} and Δ_{47}, two completely independent temperature proxies, adds
136 additional support for negligible effects of non-thermal factors on either proxy.
137
138 **Interrogating reasons for discrepancies between temperature estimates**
139 Mg/Ca- and Δ_{47}-based paleotemperatures have both been measured on the tests of
140 *G. bulloides* from the same sediment core. The offsets in reconstructed temperature between
141 these proxies can thus not be explained by sampling, seasonality and/or depth habitat of the
142 foraminiferal species (Supplementary Fig. S7). The offsets can also not be explained by
143 variations in seawater Mg/Ca, potentially affecting the use of Mg/Ca paleothermometry on
144 longer timescales (>1 Myr)[31,32]. We furthermore consider the effects of regional changes in
145 salinity, dissolution and diagenesis as unlikely explanations for the observed temperature
146 divergence between the two foraminifera-based proxies (see additional discussions in the
147 Supplementary Information). Instead, a larger-scale influence on Mg/Ca is suggested by the
148 observation that the stepped temperature decrease reconstructed from Mg/Ca at Site 1171 is
149 mirrored by other planktic foraminiferal Mg/Ca-based temperature records in the Atlantic and

150 Pacific sectors of the Southern Ocean[9,10]. We propose that, while all proxies agree on cooling
151 across the MMCT, the abruptness and the larger magnitude of the cooling in Mg/Ca
152 compared to Δ_{47} and TEX_{86} temperatures may primarily result from the pronounced increase
153 in global surface ocean pH, which is linked to a decline in atmospheric CO_2[2].
154
155 To test this hypothesis, we examine the magnitude of pH change required to bring all
156 paleotemperature estimates from Site 1171 into agreement. We derive relative changes in pH
157 from foraminiferal Mg/Ca signatures based on recent empirical evidence of the pH effect on
158 *G. bulloides* Mg/Ca[12], after accounting for the temperature signal inferred from either Δ_{47} or
159 TEX_{86} (Fig. 3). Our calculated relative pH values are consistent with a compilation of boron
160 isotope ($\delta^{11}B$)-based pH reconstructions from various sites[2]. The apparently larger and more
161 abrupt increase in pH suggested by our calculations could be related to the limited temporal
162 coverage of $\delta^{11}B$-based records (e.g., data gap between ~14.8 Ma and ~14.1 Ma),
163 uncertainties in the exact strength of the pH effect on Mg/Ca[12,13], additional effects on the
164 temperature proxies and/or regional hydrographic controls at Site 1171 (Supplementary
165 Information). In any case, the previously reconstructed fluctuations in global pH[2] seem to be
166 sufficient to explain the diverging trends between previous Mg/Ca-based temperature
167 estimates[9,33] and our new Δ_{47}- and TEX_{86}-derived temperature records. A pH effect on Mg/Ca
168 may not be an exclusive feature of *G. bulloides*; other widely used planktic foraminiferal
169 species such as *Globigerinoides ruber* also tend to show some sensitivity to pH[12,34].
170 Therefore, assuming temperature as the only control on Mg/Ca in the tests of these species
171 can potentially lead to a significant bias in the timing and magnitude of estimated temperature
172 change across climate transitions that are characterized by large changes in atmospheric CO_2
173 (such as the MMCT).

Implications for middle Miocene climate change

The substantial lead of Mg/Ca-based upper ocean cooling and salinity decrease in the Southern Ocean (starting between 14.2 and 14.1 Ma) versus Antarctic ice sheet expansion (14.0-13.7 Ma according to benthic foraminiferal $\delta^{18}O$, Fig. 2) has previously been related to a decoupling of Southern Ocean surface hydrography and global ice volume, caused by circulation changes and/or thresholds for Antarctic ice growth[9,10]. In apparent contrast to these studies, our multiproxy upper ocean temperature record from Site 1171 has a temporal structure much more similar to that of benthic $\delta^{18}O$ from the same site (Fig. 4a). This observation provides evidence for a coupling of upper ocean temperature in the Southern Ocean with the increase in Antarctic ice volume, suggesting a direct mechanistic connection between Southern Ocean and Antarctica and/or a common universal driver for climate change at high southern latitudes, such as a decline in CO_2.

The exact timing of the CO_2 decrease across the MMCT is currently uncertain in the available $\delta^{11}B$-based reconstructions, hampering assessment of potential leads and lags between CO_2 forcing and climate response (Fig. 3a). Higher-resolution $\delta^{11}B$ records are needed to provide a more detailed reconstruction of pH and CO_2. However, in the case that the Mg/Ca temperature bias was indeed primarily caused by an increase in global surface ocean pH (Fig. 3b), the middle Miocene decrease in atmospheric CO_2[1–3] would have been broadly synchronous with the observed upper ocean cooling and cryosphere expansion. Such a synchronicity in timing is consistent with atmospheric CO_2 playing an important role in the Antarctic ice sheet expansion, although additional forcing factors and feedbacks were likely also involved. The abrupt increase in ice volume may have been reinforced by an orbital configuration that caused low seasonality over Antarctica[11] and/or tectonic processes (e.g., via

198 Antarctic bedrock topography and gateway configurations), while snow and ice albedo
199 feedbacks likely encouraged further ice sheet growth during the MMCT[9].
200
201 The reconstructed temperatures can be used to estimate seawater $\delta^{18}O$ in combination with
202 *G. bulloides* $\delta^{18}O$, and to derive local variations in salinity after accounting for changes in
203 global ice volume (Methods). The results suggest a decrease in upper ocean salinity coupled
204 to the expansion of the Antarctic ice sheet, with the magnitude of the salinity decrease
205 depending on the amount of ice growth (Fig. 4b and c). In combination with the inferred
206 cooling, this salinity decrease can be interpreted as a shift from saline, warm subtropical to
207 fresher and colder subantarctic conditions due to an intensification and/or northward
208 expansion of the ACC (including the Subtropical Convergence and other Southern Ocean
209 frontal systems), and possibly a northward shift in westerly winds[9,10,28]. We note that the
210 timing of our salinity reconstruction again contrasts with Mg/Ca-based evidence, which
211 would suggest that Southern Ocean salinity decrease preceded ice sheet growth by ~100-
212 300 kyr[9,10]. The proposed changes in Southern Ocean hydrography, coinciding with ice sheet
213 expansion, may have contributed to the observed CO_2 drawdown. In analogy to glacial
214 periods during the Pleistocene, a northward shift of ocean fronts and westerly winds may have
215 reduced Southern Ocean upwelling, providing a mechanism to increase deep-ocean carbon
216 storage[35–37]. Such an increase in deep-ocean CO_2 sequestration could have contributed to the
217 observed middle Miocene decline in atmospheric CO_2[1–3], regardless of the exact mechanism
218 triggering Antarctic ice sheet and ACC frontal system expansion. Our data, including relative
219 changes in pH derived from the observed discrepancies between the temperature proxies, are
220 consistent with the interpretation of a decline in atmospheric CO_2 driving Antarctic ice sheet
221 expansion during the MMCT. Alternatively, the ice sheet could have initially responded to
222 another trigger mechanism (e.g., orbital or tectonic forcing), leading to Southern Ocean

223 cooling and a northward expansion of the frontal systems, possibly (further) decreasing
224 atmospheric CO_2 through enhanced sequestration of CO_2 in the ocean interior. The hypothesis
225 of an increase in deep-ocean CO_2 sequestration in the Southern Ocean could be tested with
226 additional Southern Ocean records of marine productivity and nutrient consumption[38].
227
228 The temperature records reported here represent a change in the current view of Southern
229 Ocean temperature evolution across the MMCT, with important implications for our
230 understanding of the feedback mechanisms that controlled the evolution of the Antarctic ice
231 sheet. The temporal correspondence of the upper ocean temperature decline with ice sheet
232 expansion indicates a close coupling of Southern Ocean temperature and Antarctic ice
233 volume, challenging the notion of a lagged ice sheet response due to additional feedbacks[9].
234 Instead, the results of this study are consistent with a more direct role of atmospheric CO_2 in
235 driving the MMCT.
236
237
238 **References**

239 1. Ji, S. C. *et al.* A symmetrical CO_2 peak and asymmetrical climate change during the
240 middle Miocene. *Earth Planet. Sci. Lett.* **499**, 134–144 (2018).

241 2. Sosdian, S. M. *et al.* Constraining the evolution of Neogene ocean carbonate chemistry
242 using the boron isotope pH proxy. *Earth Planet. Sci. Lett.* **498**, 362–376 (2018).

243 3. Super, J. R. *et al.* North Atlantic temperature and pCO_2 coupling in the early-middle
244 Miocene. *Geology* **46**, 519–522 (2018).

245 4. Flower, B. P. & Kennett, J. P. Middle Miocene Ocean-Climate Transition - High-
246 Resolution Oxygen and Carbon Isotopic Records from Deep-Sea Drilling Project Site

588A, Southwest Pacific. *Paleoceanography* **8**, 811–843 (1993).

5. Zachos, J. C., Pagani, M., Sloan, L., Thomas, E. & Billups, K. Trends, rhythms, and aberrations in global climate 65 Ma to present. *Science* **292**, 686–693 (2001).

6. de Boer, B., van de Wal, R. S. W., Bintanja, R., Lourens, L. J. & Tuenter, E. Cenozoic global ice-volume and temperature simulations with 1-D ice-sheet models forced by benthic $\delta^{18}O$ records. *Ann. Glaciol.* **51**, 23–33 (2010).

7. Lear, C. H., Mawbey, E. M. & Rosenthal, Y. Cenozoic benthic foraminiferal Mg/Ca and Li/Ca records: Toward unlocking temperatures and saturation states. *Paleoceanography* **25**, 1–11 (2010).

8. Frigola, A., Prange, M. & Schulz, M. Boundary conditions for the Middle Miocene Climate Transition (MMCT v1.0). *Geosci. Model Dev.* **11**, 1607–1626 (2018).

9. Shevenell, A. E., Kennett, J. P. & Lea, D. W. Middle Miocene Southern Ocean Cooling and Antarctic Cryosphere Expansion. *Science* **305**, 1766–1770 (2004).

10. Kuhnert, H., Bickert, T. & Paulsen, H. Southern Ocean frontal system changes precede Antarctic ice sheet growth during the middle Miocene. *Earth Planet. Sci. Lett.* **284**, 630–638 (2009).

11. Holbourn, A., Kuhnt, W., Schulz, M. & Erlenkeuser, H. Impacts of orbital forcing and atmospheric carbon dioxide on Miocene ice-sheet expansion. *Nature* **438**, 483–487 (2005).

12. Gray, W. R. & Evans, D. Nonthermal Influences on Mg/Ca in Planktonic Foraminifera: A Review of Culture Studies and Application to the Last Glacial Maximum. *Paleoceanogr. Paleoclimatol.* **34**, 1–10 (2019).

13. Holland, K. *et al.* Constraining multiple controls on planktic foraminifera Mg/Ca. *Geochim. Cosmochim. Acta* **273**, 116–136 (2020).

14. Exon, N. F., Kennett, J. P., Malone, M. J. & the Expedition 189 Scientists. Site 1171. in *Proceedings of the Ocean Drilling Program, Initial Reports Volume 189* (2001).

15. Ghosh, P. *et al.* ^{13}C-^{18}O bonds in carbonate minerals: A new kind of paleothermometer. *Geochim. Cosmochim. Acta* **70**, 1439–1456 (2006).

16. Peral, M. *et al.* Updated calibration of the clumped isotope thermometer in planktonic and benthic foraminifera. *Geochim. Cosmochim. Acta* **239**, 1–16 (2018).

17. Leutert, T. J. *et al.* Sensitivity of clumped isotope temperatures in fossil benthic and planktic foraminifera to diagenetic alteration. *Geochim. Cosmochim. Acta* **257**, 354–372 (2019).

18. Meinicke, N. *et al.* A robust calibration of the clumped isotopes to temperature relationship for foraminifers. *Geochim. Cosmochim. Acta* **270**, 160–183 (2020).

19. Schouten, S., Hopmans, E. C., Schefuss, E. & Damsté, J. S. S. Distributional variations in marine crenarchaeotal membrane lipids: a new tool for reconstructing ancient sea water temperatures? *Earth Planet. Sci. Lett.* **204**, 265–274 (2002).

20. Schouten, S., Hopmans, E. C. & Damsté, J. S. S. The organic geochemistry of glycerol dialkyl glycerol tetraether lipids: A review. *Org. Geochem.* **54**, 19–61 (2013).

21. Elling, F. J., Konneke, M., Mussmann, M., Greve, A. & Hinrichs, K. U. Influence of temperature, pH, and salinity on membrane lipid composition and TEX_{86} of marine planktonic thaumarchaeal isolates. *Geochim. Cosmochim. Acta* **171**, 238–255 (2015).

22. Heath, R. A. A Review of the physical Oceanography of the Seas around New-Zealand

- 1982. *New Zeal. J. Mar. Freshw. Res.* **19**, 79–124 (1985).

23. Torsvik, T. H. *et al.* Phanerozoic polar wander, palaeogeography and dynamics. *Earth-Science Rev.* **114**, 325–368 (2012).

24. van Hinsbergen, D. J. J. *et al.* A Paleolatitude Calculator for Paleoclimate Studies. *PLoS One* **10**, 1–21 (2015).

25. King, A. L. & Howard, W. R. Seasonality of foraminiferal flux in sediment traps at Chatham Rise, SW Pacific: implications for paleotemperature estimates. *Deep-Sea Research I* **48**, 1687–1708 (2001).

26. Pahnke, K., Zahn, R., Elderfield, H. & Schulz, M. 340,000-year centennial-scale marine record of Southern Hemisphere climatic oscillation. *Science* **301**, 948–952 (2003).

27. Vázquez Riveiros, N. *et al.* Mg/Ca thermometry in planktic foraminifera: Improving paleotemperature estimations for *G. bulloides* and *N. pachyderma* left. *Geochem. Geophys. Geosystems* **17**, 1249–1264 (2016).

28. Sangiorgi, F. *et al.* Southern Ocean warming and Wilkes Land ice sheet retreat during the mid-Miocene. *Nat. Commun.* **9**, 1–11 (2018).

29. Knorr, G. & Lohmann, G. Climate warming during Antarctic ice sheet expansion at the Middle Miocene transition. *Nat. Geosci.* **7**, 376–381 (2014).

30. Ho, S. L. & Laepple, T. Flat meridional temperature gradient in the early Eocene in the subsurface rather than surface ocean. *Nat. Geosci.* **9**, 606–610 (2016).

31. Evans, D. & Müller, W. Deep time foraminifera Mg/Ca paleothermometry: Nonlinear correction for secular change in seawater Mg/Ca. *Paleoceanography* **27**, 1–11 (2012).

313 32. Lear, C. H. *et al.* Neogene ice volume and ocean temperatures: Insights from infaunal
314 foraminiferal Mg/Ca paleothermometry. *Paleoceanography* **30**, 1437–1454 (2015).

315 33. Shevenell, A. E., Kennett, J. P. & Lea, D. W. Southern Ocean Middle Miocene
316 ODP1171 Foraminifer Stable Isotope and Mg/Ca Data. *IGBP PAGES/World Data*
317 *Center for Paleoclimatology Data Contribution Series #2006-061* (2006).

318 34. Gray, W. R. *et al.* The effects of temperature, salinity, and the carbonate system on
319 Mg/Ca in Globigerinoides ruber (white): A global sediment trap calibration. *Earth*
320 *Planet. Sci. Lett.* **482**, 607–620 (2018).

321 35. Toggweiler, J. R., Russell, J. L. & Carson, S. R. Midlatitude westerlies, atmospheric
322 CO_2, and climate change during the ice ages. *Paleoceanography* **21**, 1–15 (2006).

323 36. Anderson, R. F. *et al.* Wind-Driven Upwelling in the Southern Ocean and the Deglacial
324 Rise in Atmospheric CO_2. *Science* **323**, 1443–1448 (2009).

325 37. Sigman, D. M., Hain, M. P. & Haug, G. H. The polar ocean and glacial cycles in
326 atmospheric CO_2 concentration. *Nature* **466**, 47–55 (2010).

327 38. Studer, A. S. *et al.* Antarctic Zone nutrient conditions during the last two glacial cycles.
328 *Paleoceanography* **30**, 845–862 (2015).

329 39. Müller, R. D. *et al.* GPlates: Building a Virtual Earth Through Deep Time. *Geochem.*
330 *Geophys. Geosystems* **19**, 2243–2261 (2018).

331 40. Matthews, K. J. *et al.* Global plate boundary evolution and kinematics since the late
332 Paleozoic. *Glob. Planet. Change* **146**, 226–250 (2016).

333 41. Bernasconi, S. M. *et al.* Reducing uncertainties in carbonate clumped isotope analysis
334 through consistent carbonate-based standardization. *Geochem. Geophys. Geosystems*

19, 2895–2914 (2018).

42. Kele, S. *et al.* Temperature dependence of oxygen- and clumped isotope fractionation in carbonates: A study of travertines and tufas in the 6–95 °C temperature range. *Geochim. Cosmochim. Acta* **168**, 172–192 (2015).

43. Kim, J. H. *et al.* New indices and calibrations derived from the distribution of crenarchaeal isoprenoid tetraether lipids: Implications for past sea surface temperature reconstructions. *Geochim. Cosmochim. Acta* **74**, 4639–4654 (2010).

44. Greenop, R. *et al.* A record of Neogene seawater $\delta^{11}B$ reconstructed from paired $\delta^{11}B$ analyses on benthic and planktic foraminifera. *Clim. Past* **13**, 149–170 (2017).

Acknowledgements

We thank Amelia Shevenell, David Evans, Gavin Foster and Alvaro Fernandez Bremer for insightful discussions, and Enver Alagoz, Irene Heggstad and Mareike Schmitt for laboratory assistance. Furthermore, we thank all authors who shared their published data. This research used data and samples provided by the International Ocean Discovery Program (IODP) and its predecessor, the Ocean Drilling Program (ODP). This work was funded by the European Research Council (ERC) under the European Union's Horizon 2020 research and innovation programme (grant agreement No 638467), the Trond Mohn Foundation and the Max Planck Society.

356 **Corresponding author**

357 Correspondence and requests for materials should be addressed to Thomas Jan Leutert
358 (corresponding author, e-mail: Thomas.Leutert@mpic.de).

359

360

361 **Author contribution statement**

362 T.J.L. and A.N.M. initiated and designed the study. T.J.L. generated and analysed clumped
363 isotope data under the oversight of A.N.M. A.A. and A.M.-G. contributed TEX_{86} data and
364 their interpretation. GDGT measurements were performed by A.A. under the supervision of
365 A.M.-G. All authors contributed to paleoceanographic interpretation. T.J.L. wrote the paper
366 with significant contributions from A.N.M., A.A., A.M.-G. and S.M.

367

368

369 **Competing interests**

370 The authors declare no competing interests.

371

372

373 **Data availability**

374 The clumped isotope and TEX_{86} temperature data that support the findings of this study are
375 available in the Supplementary Information and at Pangaea
376 (https://doi.org/10.1594/PANGAEA.919353, https://doi.org/10.1594/PANGAEA.919351).
377 The full raw isotope data is published on the EarthChem Database
378 (https://doi.org/10.26022/IEDA/111547).

379

380 **Figure Captions**

381 **Fig. 1: Site map and paleogeographic reconstruction.** The modern location of ODP
382 Site 1171[9,14] on the South Tasman Rise is shown with a black circle. Dashed black lines
383 schematically indicate modern positions of Subtropical Convergence (STC), Subantarctic
384 Front (SAF) and Antarctic Polar Front (AAPF). Site 1171 location and coastlines at ~14 Ma
385 are indicated in white. Map created with GPlates[23,39,40].

386

387 **Fig. 2: Benthic $\delta^{18}O$ and multiproxy temperature records from ODP Site 1171 located**
388 **on the South Tasman Rise. a**, Benthic foraminiferal $\delta^{18}O$[9,33]. **b**, Upper ocean temperatures
389 from planktic foraminiferal Mg/Ca[9,33] (Gray and Evans[12] (GE) calibration) with gradually
390 changing[32] (solid line) and constant seawater Mg/Ca (3 mol/mol, dotted line). **c**, Upper ocean
391 temperatures from planktic foraminiferal Δ_{47} (this study, recalculated[41] Kele et al.[42]
392 calibration). **d**, TEX_{86} temperatures (this study) based on subsurface calibration of Ho and
393 Laepple[30] (HL, solid line, triangles) and surface calibration of Kim et al.[43] (dashed line). In **b**
394 and **d**, vertical bars indicate typical analytical errors (one standard deviation, Methods). For
395 Δ_{47} temperatures (**c**), solid horizontal lines mark averaging intervals, with symbols placed at
396 mean ages and numbers of measurements shown at the bottom (red numbers). Vertical error
397 bars in **c** represent 68% (solid vertical lines) and 95% (dashed vertical lines) confidence
398 intervals. In addition, a LOESS regression is shown (solid line, smoothing optimized by
399 generalized cross-validation). For direct comparison, Mg/Ca- and TEX_{86}-based temperatures
400 (**b**, **d**) are averaged over similar time intervals as those based on Δ_{47} (**c**). The purple bar marks
401 the onset of the decrease in Mg/Ca temperatures to visualize its lead relative to the other
402 records.

403

Fig. 3: Middle Miocene carbon cycle changes. a, Compilation of boron isotope ($\delta^{11}B$)-based reconstructions of atmospheric CO_2 including data from ODP Site 926 (tropical North Atlantic), ODP Site 761 (Indian Ocean), and the Blue Clay Formation (Malta) (see Sosdian et al.[2] and references therein), the latter two on revised age models (Supplementary Information). **b**, $\delta^{11}B$-based pH estimates from the same sites[2] (white filled symbols) compared to relative changes in pH (ΔpH) calculated from Δ_{47} (red circles, vertical lines = 68% confidence limits, horizontal lines = covered time intervals) and TEX_{86} (dark blue triangles)[12,30,41,42] in combination with Mg/Ca[9,33] (Methods). $\delta^{11}B$-based reconstructions of CO_2 (**a**) and pH (**b**) use seawater $\delta^{11}B$ from Greenop et al.[44] and Mg/Ca-based temperatures from a foraminiferal species that appears insensitive to carbonate chemistry[2,12]. Alternative scenarios of $\delta^{11}B$ yield similar changes in CO_2 and pH (Supplementary Fig. S14). Error bars for $\delta^{11}B$-based values indicate 66% confidence limits. For ΔpH data using Δ_{47} and TEX_{86} (**b**), red and dark blue shadings correspond to 68% confidence limits of generalized cross-validation-optimized LOESS fits. For ΔpH calculated from Δ_{47}, the mean LOESS fit is shown (solid red line) as well as the effects of assuming stepped salinity changes of 1 and 2 psu at 13.9 Ma (long and short dashes, respectively) and constant (3 mol/mol, instead of gradually changing[32]) seawater Mg/Ca (dotted line).

Fig. 4: Southern Ocean climate evolution during the MMCT. a, Temperature anomalies (ΔT) based on planktic foraminiferal Δ_{47} (red) and TEX_{86} (dark blue, HL calibration[30]) from ODP Site 1171 compared to benthic foraminiferal $\delta^{18}O$ from the same site[9,33] (green). **b**, Local seawater $\delta^{18}O$ ($\delta^{18}O_{sw}$) calculated from planktic foraminiferal $\delta^{18}O$[9,33] in combination with Δ_{47} (red) and TEX_{86} (dark blue) temperatures (Methods). **c**, Local anomalies in seawater $\delta^{18}O$ compared to mean ocean $\delta^{18}O$ ($\Delta\delta^{18}O_{sw}$) and inferred salinity changes (Δsalinity). $\Delta\delta^{18}O_{sw}$ represents TEX_{86}-derived $\delta^{18}O_{sw}$ with a benthic $\delta^{18}O$-based

correction for global ice volume-related changes in mean ocean $\delta^{18}O$. For this correction, we assume that 50% (orange), 70% (black) or 100% (light blue) of the change in benthic foraminiferal $\delta^{18}O$ at Site 1171[9,33] is caused by fluctuations in global ice volume (mean ocean $\delta^{18}O$)[6–8,10] (Methods). Salinity anomalies are based on a $\delta^{18}O_{sw}$-salinity relation for high southern latitudes[26]. Vertical error bars correspond to 68% confidence limits.

Methods

Study site and sampling

ODP Site 1171, located on the southernmost South Tasman Rise in the Southern Ocean (48°30'S, 149°07'E, 2150 m water depth), has been used extensively for middle Miocene paleoclimate reconstructions[9,14,33,45,46]. The sampled sediment section covering the interval from ~15.5 Ma to ~11.8 Ma (Supplementary Figs. S3 and S4) consists of carbonate-rich (~94 wt%) nannofossil ooze with foraminifera[14]. *G. bulloides* is a well-documented and widely used foraminiferal species, and is present throughout the whole sample interval. Tests of *G. bulloides* from 137 samples (30 cm^3 of sediment each) were used to generate the clumped isotope temperature record. Each sample was washed over a 63 μm sieve, dried at 50°C overnight and dry-sieved into different size fractions. Non-encrusted specimens of *G. bulloides* (Supplementary Fig. S6) were picked from the 250-355 μm size fractions, cracked between glass plates and sonicated in deionized water (3 x 10-20 seconds) and methanol (1 x 5 seconds). At the end of the cleaning procedure, test fragments were rinsed (at least three times) until the solute was no longer cloudy, and dried at 50°C.

Clumped isotope paleothermometry

The low natural abundance of ^{13}C-^{18}O bonds within carbonate ions demands large sample sizes to produce data with the precision required for paleoclimate applications. Here, we used small (~100 μg) subsamples[47–49] and obtained the necessary precision by averaging around 30 Δ_{47} measurement values from neighbouring samples[50,51]. This enables production of a low-resolution clumped isotope record in parallel with higher-resolution $\delta^{18}O$ and $\delta^{13}C$ time series (Supplementary Figs. S4 and S7), and avoids aliasing. Our planktic foraminiferal clumped isotope record consists of a total of 397 measurements (1-6 measurements per sediment sample). These measurements were performed at the University of Bergen on two Thermo Scientific MAT 253 Plus mass spectrometers connected to Thermo Scientific Kiel IV carbonate preparation devices[49,52]. Detailed analytical methods can be found in the Supplementary Information. We used four carbonate standards (ETH 1, 2, 3 and 4) differing in bulk isotopic composition and ordering state to correct and monitor the results. A 23 h-run included approximately equal numbers of carbonate standards and samples. External reproducibilities (one standard deviation) in Δ_{47} of the four carbonate standards after correction are typically 0.030-0.040‰. Carbonate $\delta^{18}O$ and $\delta^{13}C$ values are reported relative to the VPDB scale. $\delta^{18}O$ and $\delta^{13}C$ values of all standards have external reproducibilities (one standard deviation) of 0.04-0.09‰ and 0.02-0.05‰, respectively.

We utilized the Δ_{47}-temperature equation of Kele et al.[42] in the recalculated version of Bernasconi et al.[41]. This well-constrained calibration based on travertines in the range from 6°C to 95°C was derived using a very similar analytical approach as employed in this study, and agrees closely with recent foraminifera calibrations[16,18,53]. 68% and 95% confidence intervals of our clumped isotope temperatures represent fully propagated measurement and calibration uncertainties[54].

477 **TEX_{86} paleothermometry**

478 An average of 19 g of freeze-dried sediment was extracted three times using a 1:1 mixture of
479 dichloromethane (DCM) and methanol (MeOH) in Accelerated Solvent Extractor (ASE 350)
480 cells filled with 8 g of 5% deactivated silica (in hexane)[55]. After adding 60 µl of an internal
481 standard (C_{46}-GDGT), the extract was evaporated using a rocket solvent evaporator
482 (Genevac-Thermo) and subsequently filtered using a PTFE filter (0.2 µm pore size) with a
483 1.8% mixture of hexane:isopropanol (hex:IPA).
484
485 GDGTs were analyzed using an HPLC (Agilent, 1260 Infinity) coupled to a single quadrupole
486 mass spectrometer detector (Agilent, 6130) following Hopmans et al.[56]. 20 µl of sample were
487 injected, and chromatographic separation of the different GDGTs was achieved with two
488 coupled UHPLC silica columns in series (BEH HILIC columns, 2.1 150 mm, 1.7 lm; Waters)
489 maintained at 30°C. The flow rate of the 1.8% hex:IPA mobile phase was 0.2 ml/min and kept
490 constant for the first 25 min, followed by a gradient to 3.5% hex:IPA in 25 min, and a column
491 cleaning step with 10% IPA in hexane. GDGT concentrations were quantified using a C_{46}-
492 GDGT standard[57].
493
494 TEX_{86} and TEX_{86}^{H} values were calculated using the equations proposed by Schouten et al.[19]
495 and Kim et al.[43], respectively. We used various calibrations to assess TEX_{86}-based upper
496 ocean temperature trends (Supplementary Fig. S5). The precision of the entire TEX_{86}
497 analytical procedure was evaluated by repeated extractions of a monitoring standard sediment
498 in every batch of samples (obtaining a standard deviation of 0.1-0.2ºC depending on the
499 calibration used, n=10). Because of the low GDGT concentrations found at Site 1171,
500 potential linearity effects were evaluated by measuring a series of dilutions of an extract from
501 our monitoring standard sediment in each batch of samples analysed in the HPLC

(Supplementary Fig. S13). The average values (13.62ºC) and standard deviations (0.17ºC) from the measurements in the range of the reported Site 1171 values are statistically undistinguishable from the average (13.59ºC) and standard deviations (0.13ºC) of measurements performed at higher concentrations. In addition, the sediment extracts from all samples from Site 1171 were analysed two times in the HPLC-MS system (obtaining an average standard deviation of 0.3-0.6ºC depending on the calibration used). In Fig. 2d, we show average standard deviations of 0.3ºC and 0.5ºC resulting from the use of the calibrations of Ho and Laepple[30] and Kim et al.[43], respectively, to illustrate typical analytical uncertainties. Measurements below the concentration range indicated in Supplementary Fig. S13 were considered to be potentially affected by linear effects and therefore were discarded.

Mg/Ca paleothermometry and ΔpH calculations

We recalculated ocean temperatures from published Mg/Ca signatures of middle Miocene *G. bulloides* at Site 1171 using the Mg/Ca-temperature equation of Gray and Evans[12]. We modified the equation to include the Mg/Ca_{test}–Mg/Ca_{sw} relationship with the H-value described in Evans and Müller[31]:

$$T = (1 / 0.064) \times [\ln(Mg/Ca_{test} \times [Mg/Ca_{sw,0}]^{H} / [Mg/Ca_{sw,t}]^{H}) - 0.036 \times (\text{salinity} - 35) + 0.88 \times (\text{pH} - 8) - 0.15] \quad (1)$$

T is temperature in °C. $Mg/Ca_{sw,0}$ and $Mg/Ca_{sw,t}$ are present-day and past seawater Mg/Ca in mol/mol. For $Mg/Ca_{sw,0}$, we use a value of 5.2 mol/mol[31]. For $Mg/Ca_{sw,t}$, we use a recent estimate of a gradually changing value (increasing from ~2.8 mol/mol to ~3.2 mol/mol in the time interval of this study) given by a polynomial curve fit through compiled seawater Mg/Ca

proxy records[32] (solid line in Fig. 2b) as well as a constant value of 3.0 mol/mol (dotted line in Fig. 2b). For H, we use a value of 0.72, based on the calibration data reported in Evans et al.[58]. For salinity, we use a close to present-day salinity value of 34.5 psu (Supplementary Fig. S2). Due to a lack of constraint at Site 1171, we do not apply a correction for pH, but note that we solve Equation (1) for pH to calculate relative changes in pH (ΔpH) at the site. The typical analytical error in Mg/Ca temperature shown in Fig. 2b was calculated with Equation (1) using the reported pooled Hole 1171C standard deviation of replicate analyses of 7.8%[9] and a mean Mg/Ca value of 2.6 mmol/mol[9,33] (without calibration uncertainties). The sensitivity to the choice of the *G. bulloides* temperature calibration is illustrated in Supplementary Fig. S8, and the effect of assuming different seawater Mg/Ca compositions is illustrated in Supplementary Fig. S9.

In order to calculate ΔpH, we solve Equation (1) for pH:

$$\mathrm{pH} = (1 / 0.88) \times [0.036 \times (\mathrm{salinity} - 35) + 0.064 \times T + 0.15 - \ln(\mathrm{Mg/Ca_{test}} \times [\mathrm{Mg/Ca_{sw,0}}]^{H} / [\mathrm{Mg/Ca_{sw,t}}]^{H})] + 8 \quad (2)$$

We calculate pH using averaged Mg/Ca ratios ($\mathrm{Mg/Ca_{test}}$) in combination with averaged Δ_{47}-based temperatures (T, averaging intervals are illustrated as horizontal lines in Fig. 2b and c). In addition, we calculate pH based on $\mathrm{TEX_{86}}$-based T and $\mathrm{Mg/Ca_{test}}$ with the higher-resolution Mg/Ca time series interpolated to the lower resolution of our $\mathrm{TEX_{86}}$-based temperature record. Salinity, $\mathrm{Mg/Ca_{sw,0}}$, $\mathrm{Mg/Ca_{sw,t}}$ and H-value are as defined previously. Then, we calculate ΔpH by subtracting the mean pH (averaged over all values) from each pH value. 68% confidence intervals represent the Monte Carlo-propagated uncertainties for our estimates of ΔpH. For both Δ_{47}- and $\mathrm{TEX_{86}}$-based ΔpH, we generated 10,000 realizations of

552 the time series and assumed normal distribution of errors. Then, we fitted LOESS curves to
553 each realization (degree of smoothing optimized by generalized cross-validation), and
554 calculated the 68% confidence intervals (as given by the 16 and 84 percentiles) from these
555 LOESS fits. For Δ_{47}-based ΔpH, the full temperature error, the measurement error in
556 foraminiferal Mg/Ca (as given by the standard error of each calculated mean Mg/Ca value)
557 and an error of seawater Mg/Ca (0.5 mol/mol[32]) were propagated. Here, 68% confidence
558 intervals were also calculated without applying LOESS fitting (red error bars in Fig. 3b). For
559 TEX_{86}-based ΔpH, we applied a conservative estimate of the full TEX_{86} temperature error of
560 3ºC[30,59], a Mg/Ca measurement error of 0.2 mmol/mol (from the reported pooled Hole 1171C
561 standard deviation of replicate analyses of 7.8%[9] and a mean Mg/Ca value of
562 2.6 mmol/mol[9,33]) and a seawater Mg/Ca error of 0.5 mol/mol[32] for error propagation. We did
563 not include Mg/Ca calibration uncertainties in this calculation. In addition, we calculate the
564 sensitivity of calculated relative pH values to changing salinity at Site 1171 (Fig. 3b) as
565 additional influence on Mg/Ca, assuming a stepped decrease in salinity by 1 psu (from
566 35.0 psu to 34.0 psu) and 2 psu (from 35.5 psu to 33.5 psu), respectively, at 13.9 Ma.
567
568 **Seawater $\delta^{18}O$ and salinity calculations**
569 To calculate seawater $\delta^{18}O$ values, we first solve the temperature equation of Shackleton[60] for
570 seawater $\delta^{18}O$ ($\delta^{18}O_{sw}$):
571
572 $$\delta^{18}O_{sw} = (T - 16.9) / 4.0 + \delta^{18}O_{carb} \quad (3)$$
573
574 We use *G. bulloides* $\delta^{18}O$ values from this study and Shevenell et al.[9,33] ($\delta^{18}O_{carb}$) to calculate
575 $\delta^{18}O_{sw}$ (see Fig. S7 for *G. bulloides* $\delta^{18}O$ time series). We apply a correction of +0.2‰ to
576 convert from the VPDB to VSMOW scale[61]. Calcite precipitation temperatures (T) are

577 approximated from Δ_{47} as well as TEX_{86}. For Δ_{47}-based calculations, the results are averaged
578 over nearly identical time intervals (visualized with horizontal lines in Fig. 2c). For TEX_{86}-
579 based estimates of seawater $\delta^{18}O$, the high-resolution *G. bulloides* $\delta^{18}O$ record[9,33] is
580 interpolated to the lower-resolution of the TEX_{86} time series (instead of averaging across time
581 intervals).
582
583 To eliminate the global ice volume signal from seawater $\delta^{18}O$, we assume that 50%, 70% or
584 100% of the variability in benthic $\delta^{18}O$ measured at Site 1171[9,33,45] represents changes in
585 global ice volume. Benthic $\delta^{18}O$ anomalies are multiplied by 0.5, 0.7 or 1.0, interpolated and
586 then subtracted from TEX_{86}-based seawater $\delta^{18}O$ anomalies to calculate ice volume-corrected
587 seawater $\delta^{18}O$ anomalies ($\Delta\delta^{18}O$). Salinity anomalies (ΔS) at Site 1171 are estimated using a
588 seawater $\delta^{18}O$-salinity relation for high southern latitudes that is based on surface ocean data
589 from 40°S to 50°S[26,62]:
590
591 $$\Delta S = 1.465 \times \Delta\delta^{18}O \quad (4)$$
592
593 We acknowledge that Equation (4) is based on surface ocean data (top 50 m)[62], whereas
594 *G. bulloides* may have dwelled deeper (around 200 m) in the Southern Ocean. Furthermore,
595 we consider it unlikely that the present-day seawater $\delta^{18}O$-salinity relation was the same for
596 the middle Miocene. Therefore, we caution that our quantitative salinity estimates are very
597 uncertain and not a focus of our interpretation. However, the reconstructed decrease in
598 salinity across the MMCT is considered robust. Δ_{47}-based seawater $\delta^{18}O$ values corrected for
599 changes in global ice volume (not shown in Fig. 4) agree well with the corresponding TEX_{86}-
600 derived values within uncertainty, due to the good agreement of the temperature records.
601

602 **References**

603 45. Shevenell, A. E. & Kennett, J. P. Paleoceanographic Change During the Middle
604 Miocene Climate Revolution: An Antarctic Stable Isotope Perspective. in *The*
605 *Cenozoic Southern Ocean: Tectonics, Sedimentation, and Climate Change Between*
606 *Australia and Antarctica* (eds. Exon, N., Kennett, J. P. & Malone, M.) vol. 151 235–
607 252 (AGU, Washington, D. C., 2004).

608 46. Shevenell, A. E., Kennett, J. P. & Lea, D. W. Middle Miocene ice sheet dynamics,
609 deep-sea temperatures, and carbon cycling: A Southern Ocean perspective. *Geochem.*
610 *Geophys. Geosystems* **9**, 1–14 (2008).

611 47. Schmid, T. W., Radke, J. & Bernasconi, S. M. Clumped-isotope measurements on
612 small carbonate samples with a Kiel IV carbonate device and a MAT 253 mass
613 spectrometer. *Thermo Fish. Appl. Note* (2012).

614 48. Hu, B. *et al.* A modified procedure for gas-source isotope ratio mass spectrometry: the
615 long-integration dual-inlet (LIDI) methodology and implications for clumped isotope
616 measurements. *Rapid Commun. Mass Spectrom.* **28**, 1413–1425 (2014).

617 49. Meckler, A. N., Ziegler, M., Millan, M. I., Breitenbach, S. F. M. & Bernasconi, S. M.
618 Long-term performance of the Kiel carbonate device with a new correction scheme for
619 clumped isotope measurements. *Rapid Commun. Mass Spectrom.* **28**, 1705–1715
620 (2014).

621 50. Grauel, A. L. *et al.* Calibration and application of the 'clumped isotope' thermometer
622 to foraminifera for high resolution climate reconstructions. *Geochim. Cosmochim. Acta*
623 **108**, 125–140 (2013).

624 51. Rodríguez-Sanz, L. *et al.* Penultimate deglacial warming across the Mediterranean Sea

625 revealed by clumped isotopes in foraminifera. *Sci. Rep.* **7**, 1–11 (2017).

626 52. Schmid, T. W. & Bernasconi, S. M. An automated method for 'clumped-isotope'
627 measurements on small carbonate samples. *Rapid Commun. Mass Spectrom.* **24**, 1955–
628 1963 (2010).

629 53. Piasecki, A. *et al.* Application of Clumped Isotope Thermometry to Benthic
630 Foraminifera. *Geochem. Geophys. Geosystems* **20**, 1–9 (2019).

631 54. Huntington, K. W. *et al.* Methods and limitations of 'clumped' CO_2 isotope (Δ_{47})
632 analysis by gas-source isotope ratio mass spectrometry. *J. Mass Spectrom.* **44**, 1318–
633 1329 (2009).

634 55. Auderset, A., Schmitt, M. & Martínez-García, A. Simultaneous extraction and
635 chromatographic separation of *n*-alkanes and alkenones from glycerol dialkyl glycerol
636 tetraethers via selective Accelerated Solvent Extraction. *Org. Geochem.* **143**, 103979
637 (2020).

638 56. Hopmans, E. C., Schouten, S. & Damsté, J. S. S. The effect of improved
639 chromatography on GDGT-based palaeoproxies. *Org. Geochem.* **93**, 1–6 (2016).

640 57. Huguet, C. *et al.* An improved method to determine the absolute abundance of glycerol
641 dibiphytanyl glycerol tetraether lipids. *Org. Geochem.* **37**, 1036–1041 (2006).

642 58. Evans, D., Brierley, C., Raymo, M. E., Erez, J. & Müller, W. Planktic foraminifera
643 shell chemistry response to seawater chemistry: Pliocene-Pleistocene seawater Mg/Ca,
644 temperature and sea level change. *Earth Planet. Sci. Lett.* **438**, 139–148 (2016).

645 59. Cramwinckel, M. J. *et al.* Synchronous tropical and polar temperature evolution in the
646 Eocene. *Nature* **559**, 382–386 (2018).

60. Shackleton, N. J. Attainment of isotopic equilibrium between ocean water and the benthonic foraminifera genus Uvigerina: isotopic changes in the ocean during the last glacial. *Colloq. Int. du C.N.R.S.* 203–209 (1974).

61. Bemis, B. E., Spero, H. J., Bijma, J. & Lea, D. W. Reevaluation of the oxygen isotopic composition of planktonic foraminifera: Experimental results and revised paleotemperature equations. *Paleoceanography* **13**, 150–160 (1998).

62. Schmidt, G. A., Bigg, G. R. & Rohling, E. J. Global Seawater Oxygen-18 Database - v1.22. https://data.giss.nasa.gov/o18data/ (1999).

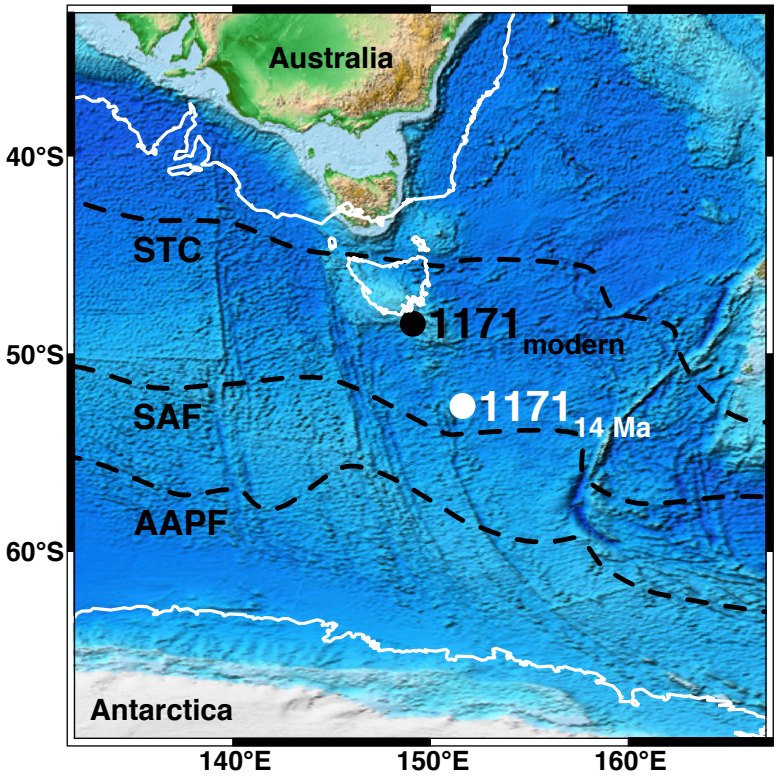
Australia
40°S
STC
1171 modern
50°S
SAF
1171 14 Ma
AAPF
60°S
Antarctica
140°E
150°E
160°E

Fig. 1

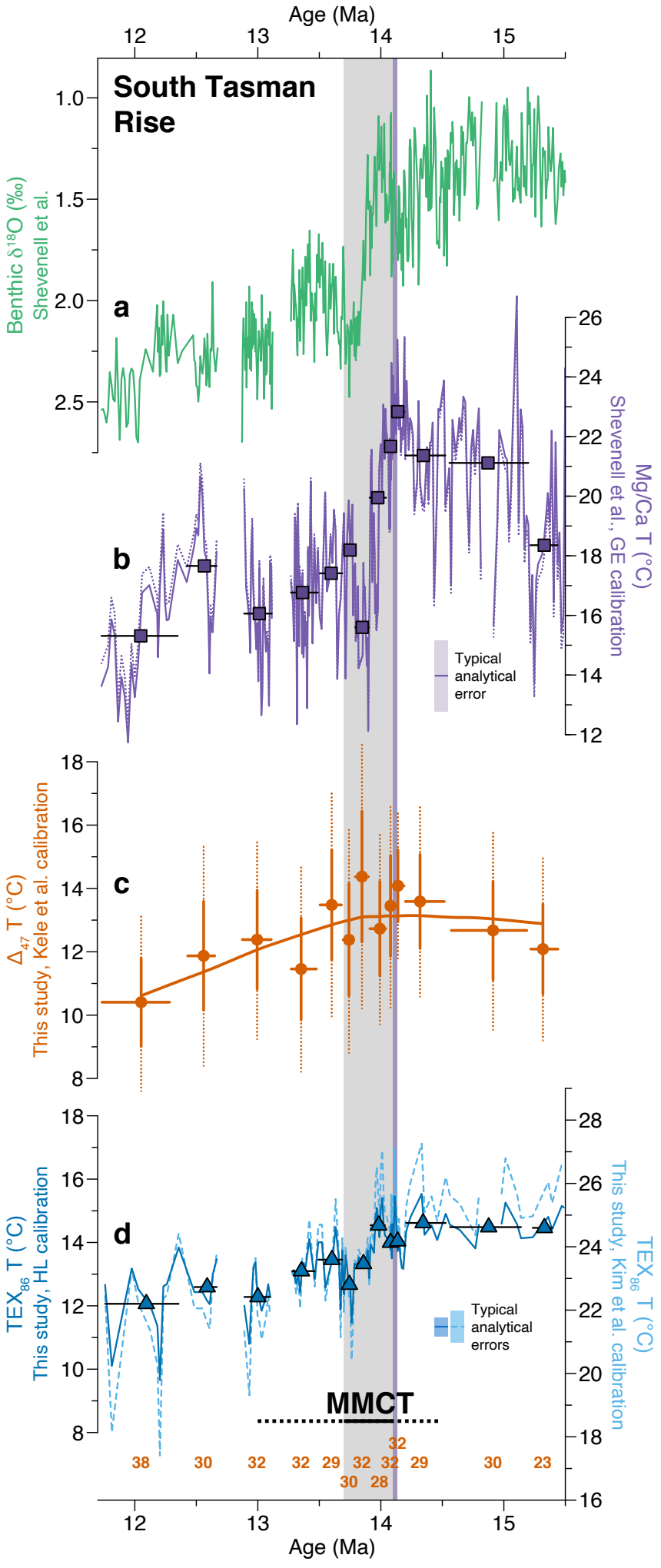
Age (Ma)
12
13
14
15
South Tasman Rise
Benthic δ18O (‰)
Shevenell et al.
1.0
1.5
2.0
2.5
a
b
Mg/Ca T (°C)
Shevenell et al., GE calibration
26
24
22
20
18
16
14
12
Typical analytical error
c
Δ47 T (°C)
This study, Kele et al. calibration
18
16
14
12
10
8
d
TEX86 T (°C)
This study, HL calibration
TEX86 T (°C)
This study, Kim et al. calibration
28
26
24
22
20
18
16
Typical analytical errors
MMCT
38
30
32
32
29
32
32
29
30
28
32
30
23
Age (Ma)

Fig. 2

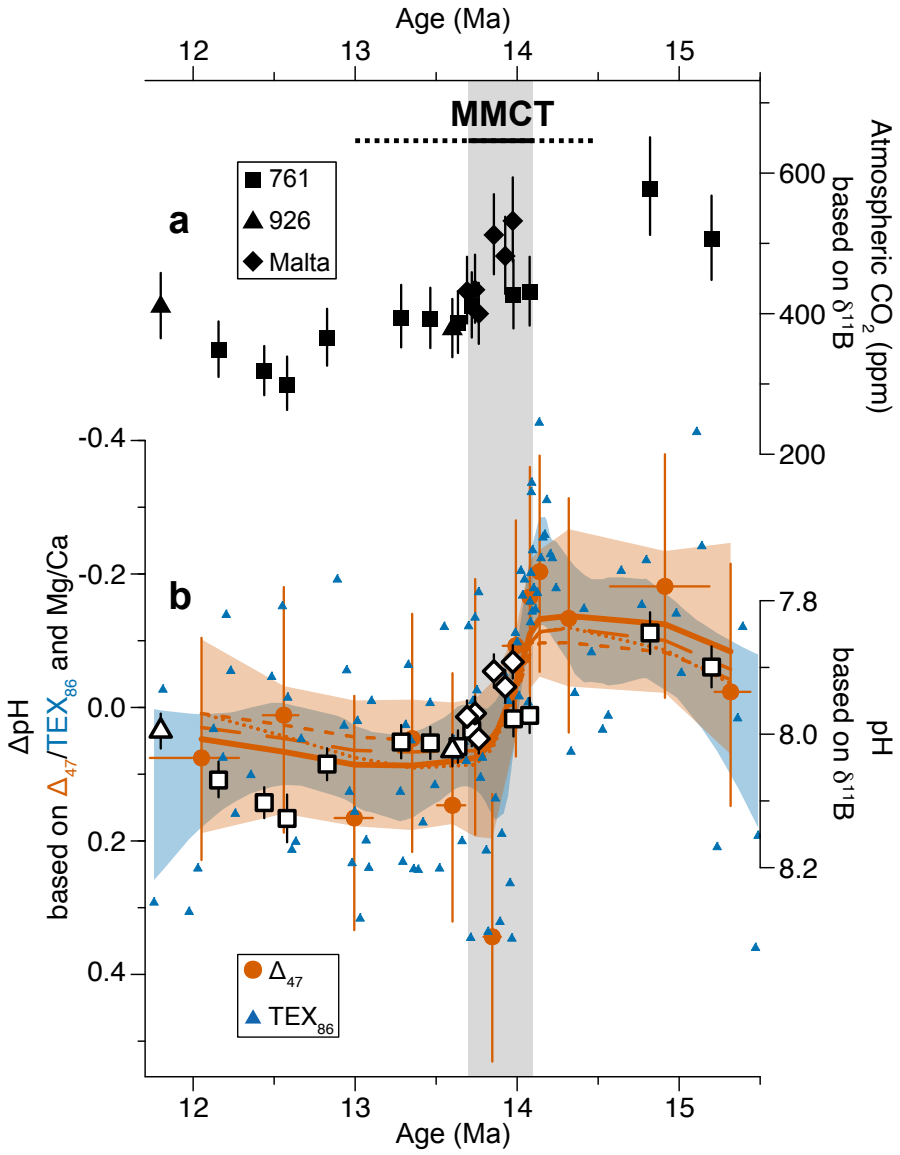
Age (Ma)
12
13
14
15
MMCT
761
926
Malta
a
b
Atmospheric CO2 (ppm)
based on δ11B
600
400
200
ΔpH
based on Δ47/TEX86 and Mg/Ca
-0.4
-0.2
0.0
0.2
0.4
pH
based on δ11B
7.8
8.0
8.2
Δ47
TEX86
Age (Ma)

Fig. 3

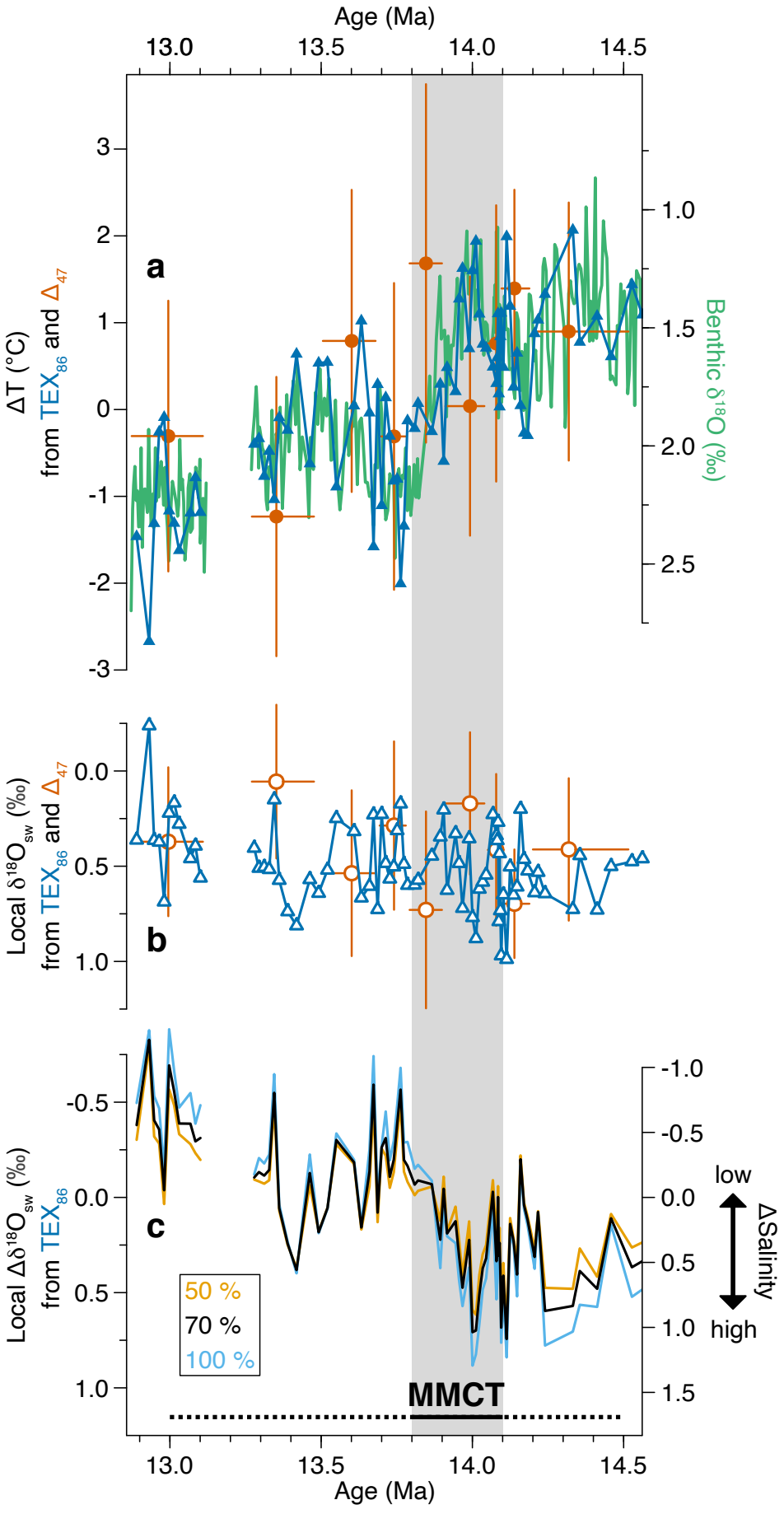
Age (Ma)
13.0
13.5
14.0
14.5
a
ΔT (°C)
from TEX86 and Δ47
Benthic δ18O (‰)
b
Local δ18Osw (‰)
from TEX86 and Δ47
c
Local Δδ18Osw (‰)
from TEX86
50 %
70 %
100 %
MMCT
low
high
ΔSalinity

Fig. 4